Design and Experimental Validation of Swirl Recovery Vanes for Propeller Propulsion Systems

Li, Qingxi; Öztürk, Kenan; Ragni, Daniele; Sinnige, Tomas; Eitelberg, Georg; Veldhuis, Leo; Yangang, Wang

DOI
10.2514/6.2017-3571

Publication date
2017

Document Version
Accepted author manuscript

Published in
35th AIAA Applied Aerodynamics Conference

This is an Accepted Manuscript of an article published in: 35th AIAA Applied Aerodynamics
Conference 5-9 June 2017, Denver, Colorado. ISBN: 978-1-62410-501-2
Available online: https://arc.aiaa.org/doi/10.2514/6.2017-3571

Design and Experimental Validation of Swirl Recovery Vanes for Propeller Propulsion Systems

Qingxi Li[1], Kenan Öztürk[2], Tomas Sinnige[3], Daniele Ragni[4], Georg Eitelberg[5], Leo Veldhuis[6]
Delft University of Technology, Delft, 2629 HS, The Netherlands

Yangang Wang[7]
Northwestern Polytechnical University, Xi'an, 710072, China

Swirl Recovery Vanes (SRVs) are a row of stationary vanes located downstream of a single-rotating propeller to recover swirl losses and thereby enhance propulsive efficiency. This paper presents the development, application, and experimental validation of a low-order SRVs design tool. The design procedure consists of three steps: first the inflow velocities can be obtained either from the simulation of isolated propeller or from experimental measurements, after which the loading distribution is defined using lifting-line theory, and lastly an airfoil design routine is performed. The design method features both a short computation time useful in the preliminary design phase and parameter investigation, and a detailed vane-shape representation, such that the final overall blade shape can be determined. In this study the model is presented together with a test example, consisting of a set of SRVs designed for a six-bladed propeller operating at high disk-loading condition. Results from the computations are subsequently experimentally validated in a wind-tunnel test of the designed model. The additional thrust generated by the SRVs was measured at different propeller loading conditions. At the design point a 2.6% increase of thrust was reported, together with a similar amount of improvement in the propeller propulsive efficiency. Velocity profiles obtained with PIV fields in the propeller slipstream were used as validation of the numerical simulation, together with quantification of the swirl recovery by SRVs.

Nomenclature

c	=	chord length, [m]	J	=	propeller advance ratio; $V_\infty/(nD)$
c_d	=	sectional drag coefficient; $d/(0.5\rho V^{*2} S)$	n	=	propeller rotation frequency, [s^{-1}]
c_r	=	propeller root chord length, [m]	N	=	vane count
C_p	=	pressure coefficient; $(p-p_\infty)/(0.5\rho V_\infty^2)$	r	=	radial coordinate, [m]
C_T	=	thrust coefficient; $T/(\rho n^2 D^4)$	R	=	propeller radius, [m]
D	=	propeller diameter, [m]	R_{SRV}	=	SRVs radius, [m]
F	=	objective function of airfoil optimization process	t	=	airfoil maximum thickness, [m]
			t_p	=	airfoil maximum thickness position, [m]
h	=	airfoil maximum camber, [m]	T_p	=	propeller thrust, [N]
h_p	=	airfoil maximum camber position, [m]	T_V	=	SRVs thrust, [N]

[1] Ph.D. candidate, Flight Performance and Propulsion Section, Faculty of Aerospace Engineering, AIAA member.
[2] M.Sc. Student, Flight Performance and Propulsion Section, Faculty of Aerospace Engineering.
[3] Ph.D. candidate, Flight Performance and Propulsion Section, Faculty of Aerospace Engineering, AIAA member.
[4] Assistant Professor, Wind Energy Section, Faculty of Aerospace Engineering, AIAA member.
[5] Full Professor, Flight Performance and Propulsion Section, Faculty of Aerospace Engineering, AIAA member.
[6] Full Professor, Head of Flight Performance and Propulsion Section, Faculty of Aerospace Engineering, AIAA member.
[7] Full Professor, School of Power and Energy, AIAA member.

v_a, v_t = axial and circumferential induced velocities by SRVs, [m·s^{-1}]
V_a, V_t = axial and circumferential inflow velocities of SRVs sections, [m·s^{-1}]
V^* = total inflow velocity of SRVs sections; $V^* = \sqrt{(V_a + v_a)^2 + (V_t + v_t)^2}$, [m·s^{-1}]
M = number of sections in SRV lifting line model
Δr = section span in SRV lifting line model
V_∞ = freestream velocity, [m·s^{-1}]
ρ = air density, [kg·m^{-3}]
α = angle of attack, [deg]
β = eddy viscosity ratio, [-]
φ = propeller phase angle, [deg]
Γ = circulation, [m^2·s^{-1}]

I. Introduction

Inspired by the world's first aviation pollution agreement and the new Airplane CO_2 Emissions Certification Standard approved by the United Nations agency Committee on Aviation Environmental Protection[1], fuel efficient propulsive systems are urgently required to lower the emissions in commercial flights. Research on open rotors has been driven by their tremendous advantages in propulsive efficiency, among which the Contra-Rotating Open Rotor configurations (CROR) are commonly considered as viable competitors to turbofan engines, due to their ability of recovering the residual swirl from the first rotor [2,3]. The torque applied by a running propeller to the fluid has a direct effect on the creation of a rotational motion in its surrounding, determining a finite swirl component in the flow. A finite amount of the shaft power is lost into fluid angular momentum and it does not result in any useful propulsive power. By recovering the swirl, extra thrust can be produced thus improving the propulsive efficiency. As illustrated by a technology-demonstrating airplane produced by Lockheed-Georgia, an 8% fuel saving and a 2.5% direct operating cost reduction were estimated for CROR engines compared to equivalent technology level turbofan engines[4]. Moreover, several control and structural benefits were observed for CROR airplanes, including a considerable reduction of torque and gyroscopic loads, and enhanced aircraft flutter stability. However, some inherent flaws of the CROR concept impose a restriction for broader application of this type of engine. Examples are the high weight of the propulsion system due to the complex gear system required for obtaining the contra rotation, the additional interaction noise of the contra-rotating stage, and the complexity of its structural layout[5].

The disadvantage of CROR can somehow be mitigated by fixing the second blade stage. In this way, the swirl-recovery benefits of CROR can still be maintained, while the complexity of the propulsion system is minimized. This approach, where the second blade stage was named Swirl Recovery Vanes (SRVs), was proposed by NASA in late 1980s. As part of the Advanced Turboprop Project[6], SRVs were designed and tested at transonic cruise conditions. Experimental data obtained at the Lewis Research Centre showed an extra thrust of 2% at the design condition of the system[7], while no additional noise was observed[8]. Despite these promising results, the research on SRVs was stopped when the energy crisis ended in the 1990s.

Recently, the SRVs concept was reintroduced by research groups at Delft University of Technology and the Northwestern Polytechnical University. In the numerical SRV design process performed by Wang et al.[9] and Stokkermans et al.[10], the vane shape was first parameterized and further optimized. In both of their work, an optimization routine was coupled with an SRVs analysis tool, of which the RANS simulation was utilized by Wang et al. and lifting line theory was applied by Stokkermans et al. The optimization results have shown an extra thrust of 2 to 5% from SRVs at high propeller-loading conditions. The unsteady interaction between the propeller and the SRVs was analyzed by Li et al.[11]. Particle-image-velocimetry (PIV) measurements conducted at DNW—LLF led to a detailed description of the flowfield induced by the propeller and SRVs, and comparisons of the aeroacoustic performance were made before and after the installation of the vanes[12].

In the SRV design work mentioned above, the process started by initialization of the geometry parameters. With an analysis tool, the performance can be obtained from the evaluations. Further on, an optimization algorithm can automate the process toward the optimum design. However, as Epps [13] shows, one can skip the intermediate "geometry" step and find the optimum design directly from the inputs. This is especially important in parametric design of SRV due to the fact that no geometry details are required at this stage. In this sense, the design process can be accelerated by direct determination of the appropriate SRV state based on the given working condition without the media of parametric geometry. Thus, a design tool is needed for the SRV with such ability.

Moreover, the inflow of SRV is highly turbulent because of the vorticity the propeller has created and the passing-by of the propeller blades, which gives a non-negligible effect compared to the normal airfoil design. With this unique working environment, the airfoil sections need to be designed specially for SRV applications.

In this paper, a hybrid design framework for the SRV is developed, which allows for both a fast computation that can be used for parameter studies and the determination of the final blade shape. Prior to the design procedure, the

isolated propeller was simulated by RANS method to provide the input velocities for SRV. From the point of view of computational efficiency for SRV design, the low-fidelity lifting line theory is adopted as it produces good prediction of blade forces and efficiency and converges quickly to optimal blade parameters such as blade number and loading distribution. In order to obtain the final blade shape, an airfoil design routine is developed and performed for several vane sections. A set of SRVs was designed for a six-bladed propeller and tested in a low-speed wind-tunnel. The measured propulsive performance of the SRVs is compared to the numerical predictions. The computed velocity profiles downstream of the propeller with and without SRVs installed are further validated by PIV measurements.

II. Design of the SRVs

A. SRV Design Procedure

The SRVs design procedure was simplified into three steps as shown in Fig. 1. At the beginning of the design, the input velocity fields need to be determined. This can be done experimentally from a wind tunnel test, or numerically from a simulation of the isolated propeller as done in the current paper. In the second step, the optimal loading distribution on the SRVs is determined. The third step then constitutes an airfoil design routine to achieve the loading distribution.

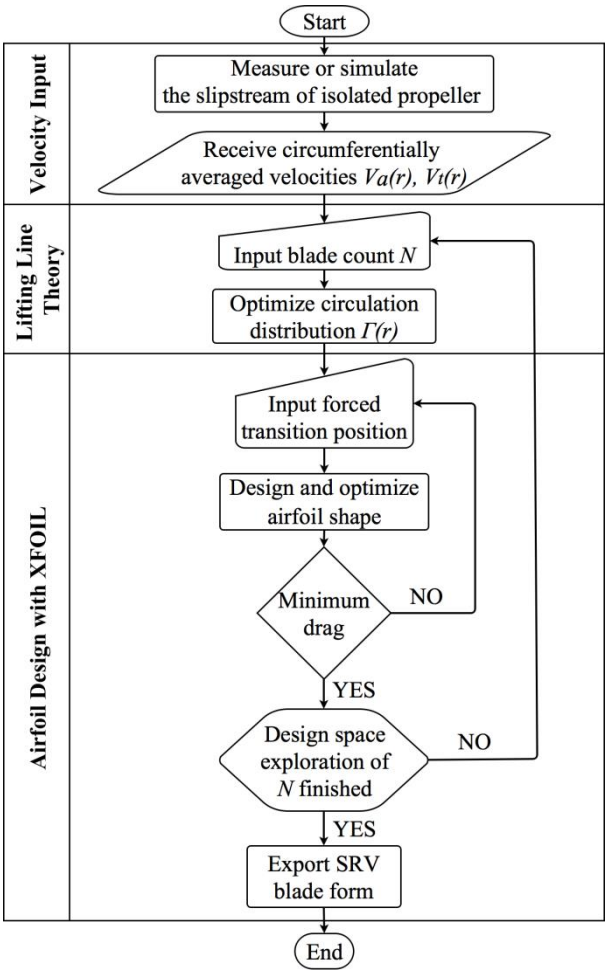

Figure 1. Framework of the SRV design procedure.

A.1. SRVs Design Input from Numerical Simulation of the Isolated Propeller

Prior to the design of the SRVs, the description of the flowfield at the position of the SRVs is required. This is achieved by performing a numerical simulation of a priori given isolated propeller based on the Reynolds-averaged Navier-Stokes (RANS) equations. The propeller used in this research represents a scaled-model of a conventional propeller of a typical regional turboprop aircraft. It features six blades and a diameter of 0.4064 m[14], as shown in Fig.

2. The hub of the propeller is 0.084 m in diameter and the blade pitch angle equals 30° at 70% of the radius. This propeller was chosen because of its availability for subsequent wind tunnel tests.

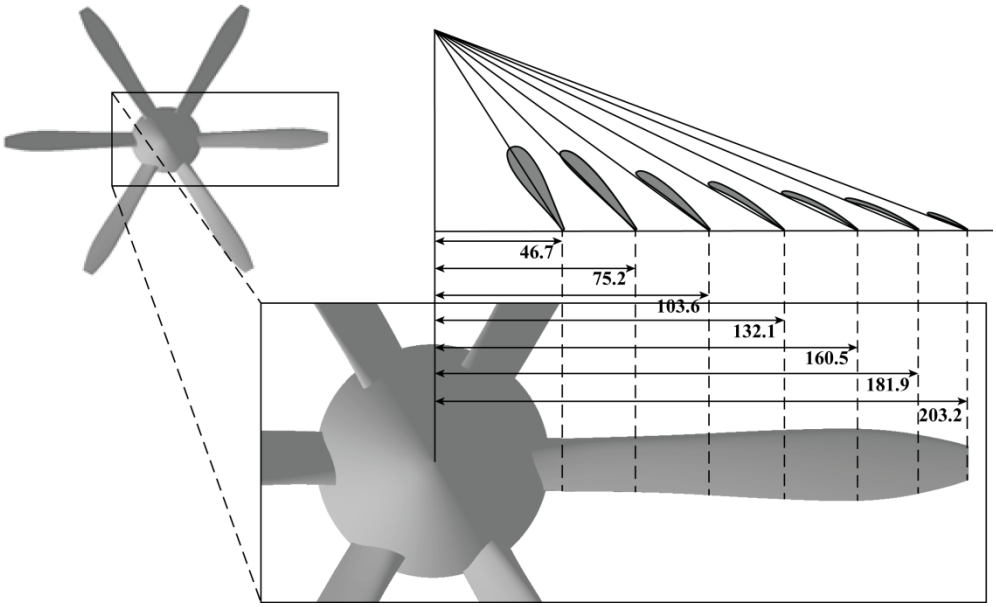

Figure 2. Propeller layout (dimensions in millimeters).

The computational domain for the propeller calculation consists of a cylinder extending about 10 times the propeller radius in all directions from the propeller-disk plane. The mesh was generated by combining two separate blocks as shown in Fig. 3. The first cylindrical block, surrounding the propeller (region I as shown in Fig. 3(a)), was generated with a structured mesh using the NUMECA® Autogrid software. Because of the symmetry of the propeller plane, only one blade sector of 60° was meshed with periodic boundary conditions. The boundary layers on the blade and hub were resolved using 25 layers of hexahedron elements. Leaving a cylindrical hole at the positon of the propeller block, the second mesh block was generated with an unstructured mesh in ANSYS® ICEM. In order to ensure an adequate resolution of the propeller slipstream at the position of the SRVs, smaller tetrahedral elements were arranged in a cylindrical area downstream of the propeller block (region Π as shown in Fig. 3(a)).

The inlet of the domain was modeled as a velocity inlet, with a turbulence intensity of 5%. A relatively high eddy viscosity ratio (β=10) was chosen. In this way, the turbulence level at the propeller plane was equal to the level of 0.5% characteristic of the wind tunnel used for the validation experiment (see Section III). At the outlet, the average static pressure was prescribed to be equal to the undisturbed static pressure. The SRV fairing, which corresponds to the curved cylinder behind the propeller as in Fig. 3(a), was taken as a no-slip wall boundary condition, thus a boundary-layer inflation layer was developed there. In contrast, the nacelle behind the SRVs fairing, which extends further downstream to the outlet, was considered as free-slip wall to reduce the number of grid points. On the sides of the computational domain, a conformal periodic boundary-condition was specified. This is possible because of the conformal mesh on these boundaries and desirable to avoid interpolation errors. The conservation equations were solved based on a rotating reference of frame, and an alternate rotation model was utilized for the advection term in the momentum equation for the purpose of error reduction.

The Shear Stress Transport (SST) turbulence model was used together with the automatic wall function to relieve the requirement for small y^+ value at wall. However, the y^+ values on the blade, hub and nacelle were still kept below 10 to capture the boundary-layer development and possible flow separation.

The simulation was performed with a freestream velocity of 29 m/s. This value was equal to the maximum value attainable in the wind tunnel used for the validation experiment (see Section III). A high loading condition of the propeller was chosen as the design point to compensate for the low freestream dynamic pressure, thus obtaining a measurable thrust on each vane. The selected operating point corresponded to a propeller advance ratio of 0.6 which leads to a thrust coefficient of C_T = 0.32, and no stall occurs along the blade.

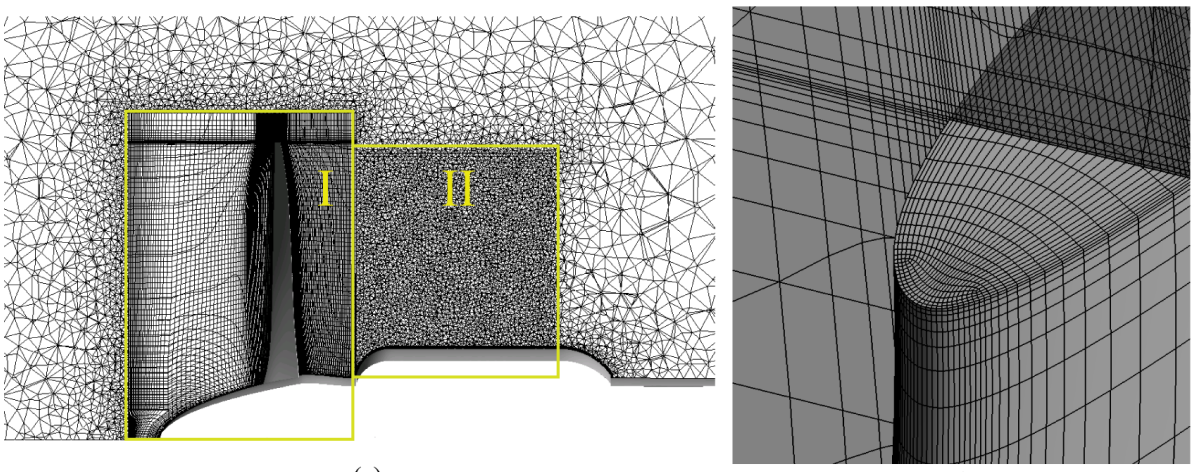

(a) (b)

Figure 3. Hybrid computation mesh for the isolated propeller; (a) blocking strategy and (b) geometry resolution shown by the local surface grid at the blade tip.

Three meshes were generated to perform a grid convergence study. The first mesh consisted of 1.55 million nodes, of which 0.88 million from the structured propeller block and 0.67 million from the unstructured nacelle one. The unstructured block was then modified to have better spatial resolution at the position of the SRVs. Combined with the same propeller block as used in the first mesh, the second mesh had a total number of 1.70 million nodes. The third mesh was up-scaled based on the first mesh in both the propeller and the nacelle blocks, with a final amount of 2.24 million nodes.

The results of the grid convergence study are presented in Fig. 4(a) in terms of the thrust coefficient of the propeller. The thrust coefficients computed using the first and second mesh both lie within 99% of the value obtained using the third fine mesh. that of the fine mesh indicating the computation convergence of all the three meshes. The radial distributions of the circumferentially-averaged axial velocity, V_a, and tangential velocity, V_t, which are critical input information for the SRV design, are compared in Fig. 4(b). The numerical velocity survey is located at the SRVs mid-chord position at $3.75c_r$ downstream of the propeller. A maximum difference of 0.36 m/s (1.2% of freestream velocity) was observed for tangential velocity between the medium and the fine mesh. The difference is 0.27 m/s (0.9% of freestream velocity) for the axial velocity. The maximum difference lies in the blade tip region as zoomed in in the figure. The reason why the computed velocities from the coarse mesh differs more from the other two meshes is due to the larger element size in the slipstream. The size of the blade tip vortex resolved by the coarse mesh is more spread out, leading to a slower decay of both the axial and the tangential velocities radially toward the outer undisturbed flow.

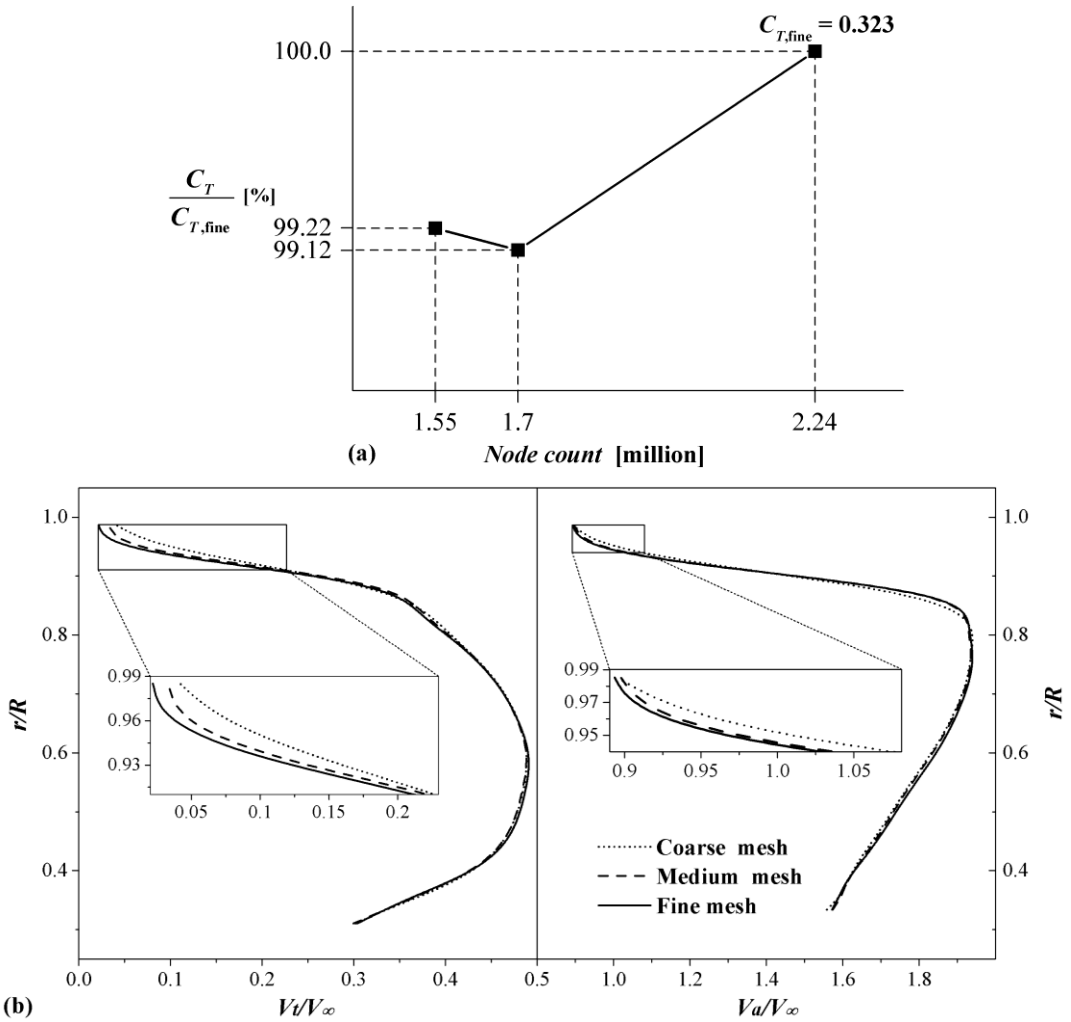

Figure 4. Grid convergence study for (a) propeller thrust coefficient and (b) circumferentially-averaged tangential and axial velocity distributions.

A.2. Determination of Circulation Distribution of SRVs

The circulation distribution is obtained with a model based on lifting-line theory as developed by Epps [15]. In this theory, the vanes are simplified into *N* lifting lines which have equal angular spacing and identical loading. The wake model of the vanes consists of constant pitch, constant radius helical vortices. The helix pitch is aligned with the total velocity at the vane position including the induced velocities. The thrust of the SRVs comes essentially from the axial component of the lift and drag acting on the vanes as:

$$T_V = \rho N \sum_{m=1}^{M} \{ [V_t + v_t] \Gamma - \frac{1}{2} V^* c_d c [V_a + v_a] \} \Delta r \tag{1}$$

In order to maximize the thrust, the partial derivative of T_V to the circulation distribution is set to zero as:

$$\begin{aligned} \frac{\partial T_V}{\partial \Gamma_i} = & \quad [V_t + v_t]_i \Delta r_i + \sum_m v_{t_m} \Gamma_m \Delta r_m \\ & - \sum_m \frac{1}{2} c_{d_m} c_m \frac{\partial V^*_m}{\partial \Gamma_i} [V_{a_m} + v_{a_m}] \Delta r_m \\ & - \sum_m \frac{1}{2} c_{d_m} c_m V^*_m v_{a_m} \Delta r_m \\ & = 0 \end{aligned} \tag{2}$$

This forms a non-linear system of equations which can be solved by a Newton method.

A.3. Airfoil Design of SRV Sections

Having determined the optimal circulation distribution from the lifting-line theory described above, the airfoil shape is designed and optimized to minimize the drag penalty of the SRVs while maintaining the desired circulation distribution. On each vane section, with the constraint of the circulation magnitude, the drag term ($c_d \cdot c$) is set as the objective function to be optimized. The airfoil geometry was parameterized using five variables: the maximum thickness *t*, position of maximum thickness t_p, maximum camber *h*, position of maximum camber h_p and chord length *c*. A robust optimization was used and two operating points were chosen in the robust optimization, i.e. the design condition where the design lift coefficient is achieved and second the stall condition where the lift coefficient starts to decrease. Given a weight factor ω_1 for the drag term at stall and another weight factor ω_2 for the stall margin; the objective function *F* is defined as:

$$F(t, t_p, h, h_p, c) = \frac{[(c_d \cdot c)_{des.}]_{opt.}}{[(c_d \cdot c)_{des.}]_{ini.}} + \omega_1 \frac{[(c_d \cdot c)_{stall}]_{opt.}}{[(c_d \cdot c)_{stall}]_{ini.}} - \omega_2 \frac{[(\alpha_{stall} - \alpha_{des.})]_{opt.}}{[(\alpha_{stall} - \alpha_{des.})]_{ini.}} \tag{3}$$

where the subscript *ini.* denotes the initial status and *opt.* the optimized results. The weight factor ω_1 and ω_2 can be chosen based on the magnitude of the inflow angle variation of individual SRV sections, and in this paper both were set to 0.5. A minimum relative thickness *t/c* of 2% was taken as a constraint to have a physically realizable blade. Initial cases were sampled randomly in the design space at the beginning of the optimization loop. A pattern search algorithm was utilized to perform the optimization, leading to fast convergence. The airfoil performance is determined from XFOIL[16], which is based on a high order panel method with a fully coupled viscous/inviscid interaction method. The corresponding Reynolds number is calculated based on the local flow parameters where the velocity term includes both the inflow velocities and the induced velocities.

B. Parametric Study of SRVs design

The parametric study was performed based on the design procedure described above. As discussed in authors' previous work[11], when the SRVs has full span of radius, the rotor tip vortex impinges periodically on the leading edge of the vane tip. The resulting unsteady loading would cause extra noise production as well as structural vibrations of the SRVs. When SRVs need to be chopped from the noise reduction point of view, the compensation on aerodynamic performance needs to be identified. Thus, investigations were carried out on the effect of vane radius and vane count on the SRVs performance.

As discussed in Section A.2, the thrust of SRVs is the result of the axial component of the lift and drag acting on the SRVs. In order to find out the theoretical maximum potential of the SRVs in terms of providing extra thrust, the drag computation was initially disabled, which means that the benefit from the SRVs would be obtained without any drag penalty. For this configuration, it can be expected that by increasing the number of vanes, more residual swirl in the propeller slipstream can be recovered due to the increased solidity. This is confirmed by the results shown in Fig. 5(a), which display the theoretical gain in thrust due to application of the SRVs as a function of the vane count. In this figure, the thrust of the SRVs was similarly non-dimensionalized by the propeller working condition as the propeller thrust coefficient. Assuming zero drag of the SRVs, the thrust increases asymptotically with the vane count, from 2.5% of the propeller thrust with 2 vanes up to 5.9% with 100 vanes. Even though it is not physically achievable, the thrust coefficient of the SRVs with 100 vanes provides an indication of the maximum thrust that SRVs can produce at the selected design condition. However, the total drag of the SRVs increases approximately linearly with the vane count. Once the increment of thrust by addition of vanes cannot compensate for the associated drag increase, any addition of vanes will reduce the final thrust and a peak occurs in this case. Therefore, an optimal vane count exists, which occurs at *N*=9. At this vane count, the predicted SRV thrust equals 4.1% of the propeller thrust when including the drag component.

The SRV performance discussed above was obtained under the condition that the radius of the SRVs is the same as that of the propeller. When reducing the vane radius, less swirl can be recovered by the SRVs. The effect of the vane radius on the SRV thrust was depicted in Fig. 5(b), where the vane count was fixed at 9. When the radius is reduced to 0.95*R*, 97% of the thrust generated by full-span (radius of the SRVs equal to that of the propeller) SRVs is obtained. From this point onward, the thrust coefficient of the SRVs decreases linearly with the reduction of the radius until 50% of the thrust for full-span SRVs at an SRV radius of 0.7 times the propeller radius.

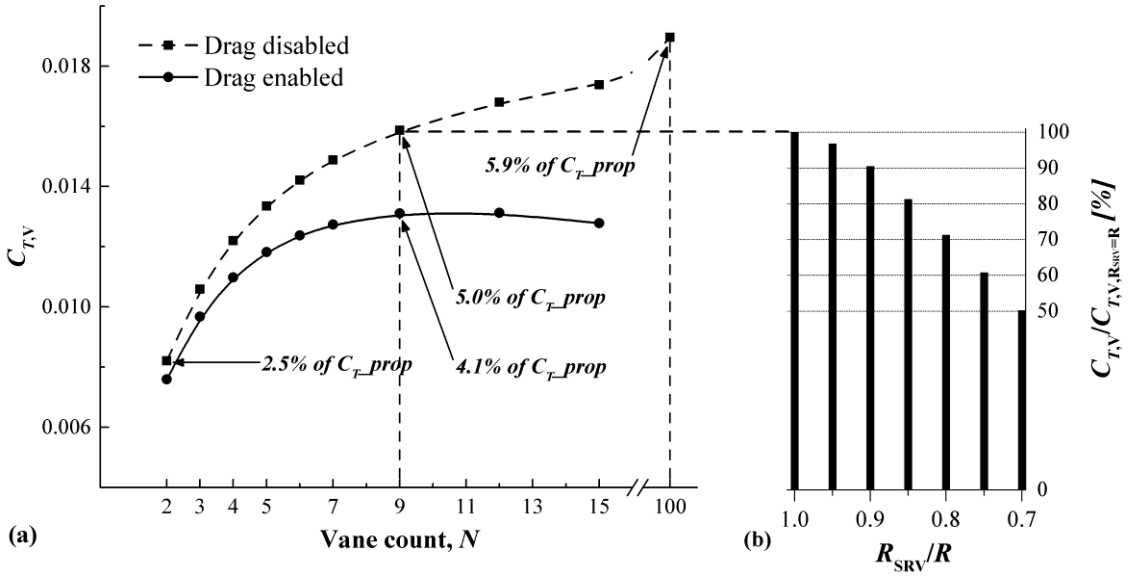

Figure 5. Parameter study for the SRVs design from the lifting-line theory based design procedure in terms of (a) vane count versus the thrust coefficient, comparison of the two lines shows the effect of taking the profile drag into account; and (b) vane radius versus the thrust coefficient at N=9.

C. SRVs Shape Design

In the experimental validation of the SRVs, there is a practical constraint that the vanes cannot be located within a certain azimuthal range on the nacelle, leaving the vane count to be 4 at maximum. Thus, for the final design used in the experimental validation study, a count of 4 was chosen instead, and the radius of the vanes equal to that of the propeller.

In the wind tunnel test where the typical Reynolds number on the vane sections is on the order of 10^5, serious deterioration of lift coefficient may occur due to the occurrence of a laminar separation bubble[17,18]. To prevent any unwanted drag increase, forced transition was used in the airfoil design. It should be noted that an instantaneous turbulent transition was assumed without any transition device drag. During the process of the airfoil optimization, an optimum forced transition position of 0.6 chord length was found to result in minimum drag on the mid-radius vane section, and this setting was implemented along all the vane sections.

The blade form curves are depicted in Fig. 6. The airfoil features a forward maximum thickness position and a backward maximum camber position, which creates a negative pressure plateau on the front part on the suction side as shown in Fig. 7. This shape of the pressure distribution resembles that of the NACA 16-series, whereas for the current airfoil there is still a pressure peak at the nose which does not occur for a NACA 16-series airfoil. Even though there is a large adverse pressure gradient from the 0.6 chord position onward on the suction side, no separation bubble occurs due to the forced transition.

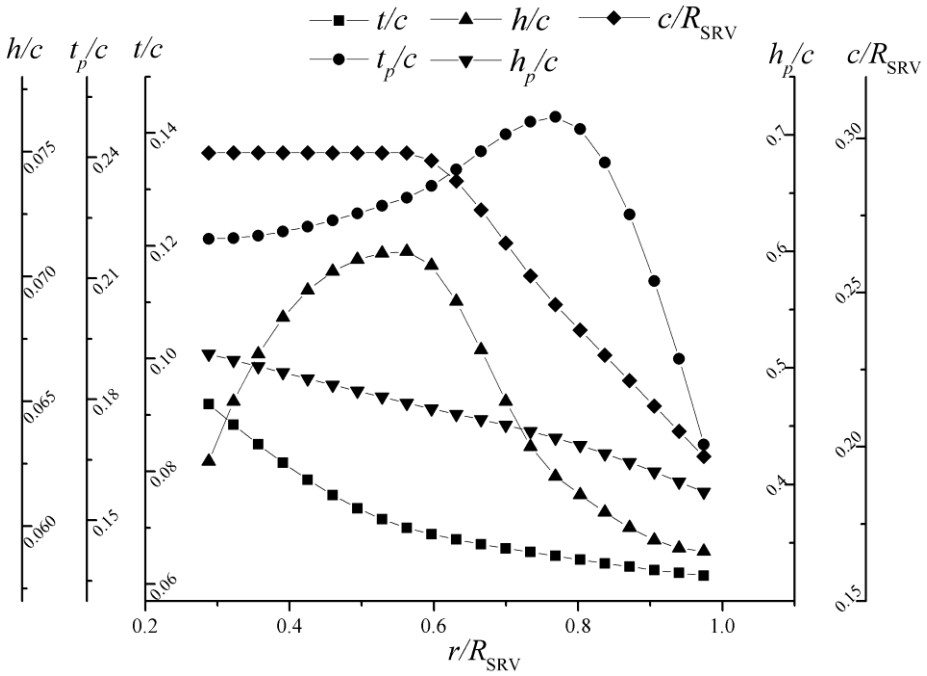

Figure 6. Blade form curves of SRVs designed with vane count *N* of 4.

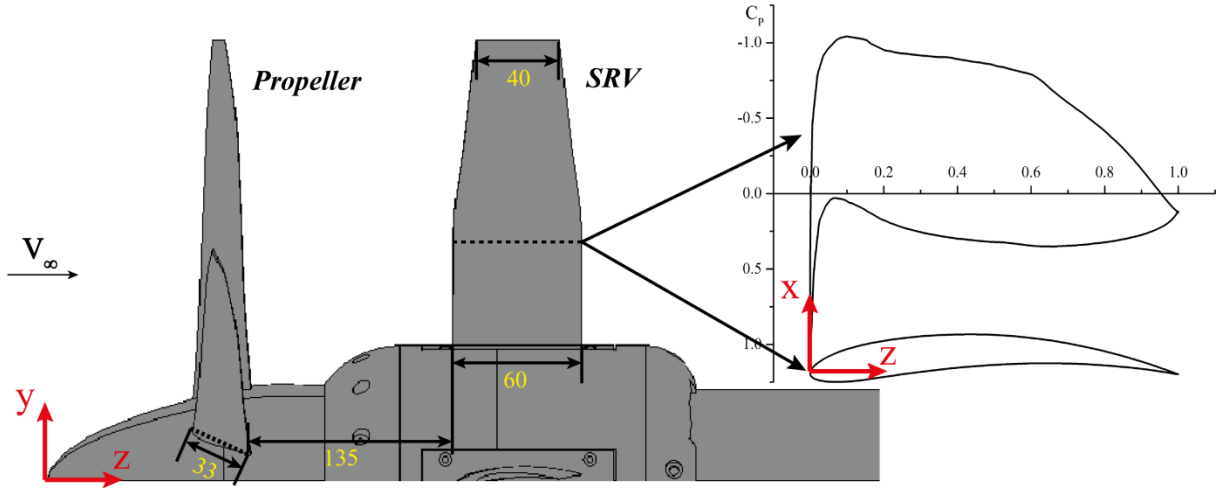

Figure 7. Sketch of the propeller, the designed SRVs and the coordinate system (dimensions in millimeters). The insert on the top right provides the airfoil shape at *r/R*=0.5 together with the predicted pressure distribution obtained from XFOIL at Re=3.15*10^5 and angle of attack of 2.5°.

III. Experimental Validation

A. Experimental Setup

Experiments were conducted on the designed SRVs together with the propeller at the low-speed open-jet wind tunnel at Delft University of Technology. The octagonal test section of the tunnel has a width and height of 2.85 m and a contraction ratio of 3:1. The model in front of the open jet is shown in Fig. 8. A honey comb flow rectifier along with five screens ensures a straightened flow with relatively low turbulence level of about 0.5% [19], and a maximum flow speed of 30 m/s can be achieved enabled by the 500kW electrical motor.

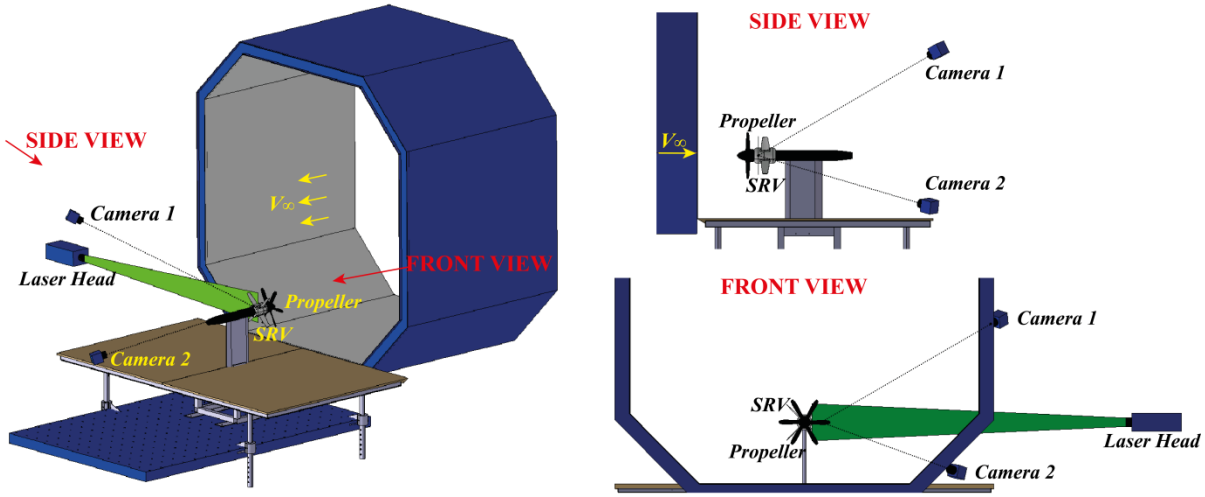

Figure 8. Sketch of the experimental setup in the Delft University OJF wind tunnel including a sketch of the PIV setup.

The propeller was driven by a Tech Development Inc. 1999 pneumatic motor. The SRVs were mounted on a sliding system which provided freedom to axial translation while constraining translation and rotation in the other five directions. A load cell was mounted in front of each vane on the sliding system measuring the axial thrust. In this way, the total thrust of the SRVs could be obtained by summation of the thrust from each individual vane. The load cell has measurement capacity of 20 N, and rated accuracy of 0.1% of full range (0.02N). The sampling frequency of the load cells were set at 5×10^5 Hz, and a total measurement time of 15 seconds was used. This corresponded to 1800 propeller revolutions at a propeller rotation frequency of 120 Hz. It should be noted that a nonzero adhesion force is always present on the sliding system whenever the vanes are producing either thrust or drag. In this respect, the load cell readings actually corresponded to the net SRV thrust minus the adhesion force, thus indicating the minimum thrust that the SRVs can produce. Since forced transition was imposed on the numerical design of the SRV platform, a zig-zag transition strip with thickness of 0.2mm was located at 0.5 chord position to guarantee a transition at 0.6 chord position on the suction side of the SRVs.

Measurements of the flowfield surrounding the SRVs were taken using stereoscopic particle-image velocimetry. A Quantel® Evergreen Nd:YAG laser with a maximum pulse energy of 200mJ was used to illuminate the particles, forming a laser sheet of about 2 mm thickness. The pulse duration is approximately 9 ns, yielding a negligible angular displacement of 3.89×10^{-4} deg based on the propeller rotation speed. Two LaVision Imager Pro LX cameras were used, with a resolution of 4870 × 3246 pixel and a pixel pitch of 7.4 μm/pixel. A lens with focal length of 200 mm was used for the lower camera, while a larger focal length (300 mm) was adopted for the upper camera to compensate for the longer distance to the measurement plane. The field of view spans around 225 × 150 mm, resulting in a digital resolution of 21.6 pixel/mm. The measurement planes were located at $0.4c_r$ upstream and downstream of the SRVs. A SAFEX® Twin Fog Double Power smoke generator was used to produce seeding particles with an average diameter of 1 μm. A total number of 1000 unconditioned image pairs were acquired and the resulting vector fields were averaged such that the measurements represent the phase-averaged results. The final integration window of 48 × 48 pixel with 75% overlap resulted in a spatial resolution of 0.55 mm.

B. Characterization of Propulsive Performance of the SRVs

The total thrust coefficient of the SRVs obtained from the load cell measurements is depicted as a function of propeller advance ratio in Fig. 9(a). It should be mentioned again that the experimental results indicated here only represent the *minimum* thrust generated by the SRVs, as discussed in Section III.A. Compared to the 3.4% of propeller thrust predicted by lifting-line theory, 2.6% was measured in the experiment for the SRVs with free transition. The additional thrust provided by the SRVs increased gradually from 0.8% at low propeller loading condition of J=1.0 up to 2.6% at the highest loading condition of J=0.55. In order to quantify the effectiveness of forced transition, measurements were then taken with the transition strip. The thrust coefficient of the SRVs exhibits a downward shift when the strip is added as can be observed from Fig. 9(b). Less thrust was generated by the SRVs with forced transition, which was caused by an increment of the drag on the vanes. In practice, there are two other reasons that may also cause transition on the SRVs other than the transition strip. First, the wakes from the propeller blades are sweeping the vanes periodically, which forms a cyclic turbulent perturbation and thus transition cycles on

the vanes, similar to the response of a wing for a wing-mounted tractor propeller[20]. Second, due to the accumulation of the particle of the seeding droplets, tiny drops perturb the outer geometry of the vanes, working as roughness hence possibly inducing early transition. Because of these reasons, transition probably also occurred without the transition strip. The same trend of thrust performance shown by the SRVs with and without forced transition also confirms that the difference is mainly from the device drag of the transition strip. With the strip installed, 2.5% of the rotor thrust was produced at the design point.

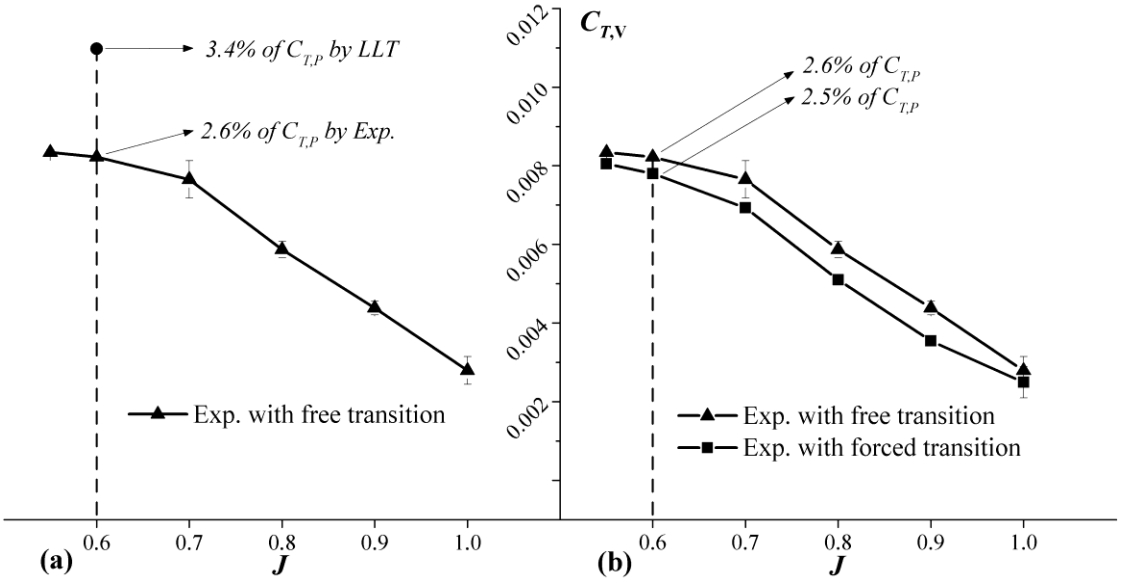

Figure 9. Propulsive characteristics of the SRVs measured using the load cell; (a) gives a comparison between the numerical design result (LLT) and experimental data (Exp.), and (b) gives a comparison of SRVs performance with free transition and forced transition obtained from experiments.

It is an intrinsic character for propeller that the slipstream exhibits a strong but periodic unsteadiness resulting from the passing-by of the blade wakes and tip vortices. As a consequence, the propulsive performance of the SRVs demonstrates severe fluctuations corresponding to the periodic inflow conditions. As an example, the unsteadiness of $C_{T,V}$ at J=0.6 for the SRVs without transition strip is shown in Fig. 10(a) for one propeller revolution. With the sampling frequency of the load cell at 5×10^5 Hz and propeller rotation frequency at 120 Hz, the measurements have a spatial resolution of 0.9°. At each propeller phase angle, results were averaged among the 1800 samples which is shown as the solid line in Fig. 10(a). Assuming the load cell reading at each propeller phase angle to have a normal distribution, the confidence interval with 95% confidence level would lie within 1.96 times the standard deviation around the mean value. This is depicted as the gray area in Fig. 10(a). Six peaks are observed in the time-dependent thrust coefficient. These are the direct results of the periodic impingement of the wakes and tip vortices of the six propeller blades on the SRVs. In the wake of the propeller blade, the velocity deficit in axial direction as well as the velocity increase in the tangential direction lead to an increase in angle of attack experienced by the downstream SRVs, and thus a spike in the thrust coefficient.

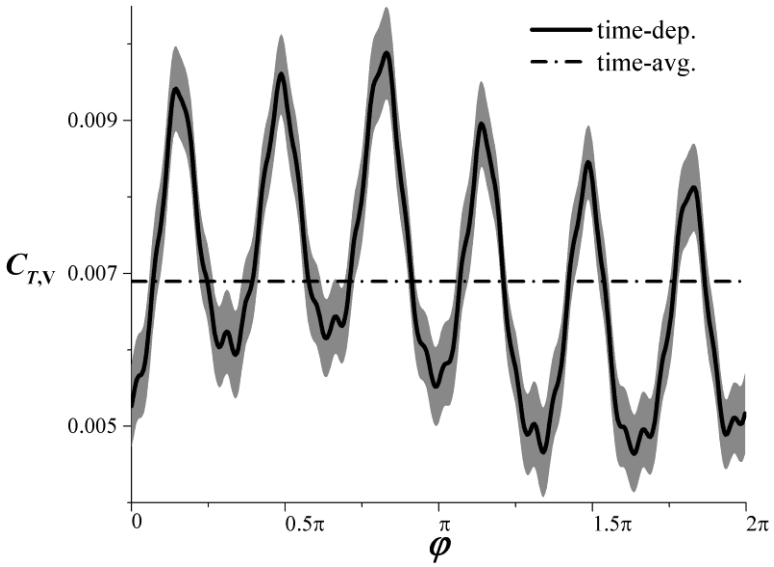

Figure 10. Unsteady propulsive performance of SRVs at J=0.6 without transition strip from load cell measurements; change of the thrust coefficient within one propeller revolution with the uncertainty shown as the gray area at 95% confidence level.

C. Flowfield Description by PIV Measurements

The input velocities from the RANS simulation of the propeller were validated by the PIV measurements on two vertical measurement planes. Figure 11 compares the circumferentially-averaged axial and tangential velocity profiles as measured in the experiment with the results obtained from the RANS simulation. The axial positions of the measurement planes are indicated by the red dashed lines. On the first plane, good agreement was observed both in the general profile shape and the magnitude between the RANS simulation and the measured data for both the tangential and the axial velocities. The maximum difference between the experimental and numerical results was 1.1 m/s, corresponding to 3.8% of the freestream velocity. On the second plane, this observation also applies for the axial velocity, but in terms of the circumferential velocity a slightly larger difference is visible. This is attributed to the coarser mesh density on this plane when referring back to Fig. 3 since the second plane is outside of the dense grid region arranged for SRV.

The recovered swirl achieved by the SRVs was also quantified by the PIV measurements as shown in Fig. 12. On the plane upstream of the SRVs, no obvious change was observed after the installation of the SRVs. At this position, the flowfield can only be affected by the vanes due to potential flow effects, but the plane was far enough away from the SRVs to make this noticeable. From this observation, it can also be expected that the installation of the SRVs has negligible influence on the propeller performance. In the plane downstream of the SRVs, the swirl is reduced and the amount of the swirl recovery increases linearly towards the nacelle. When integrated along the radius, 42% of the angular momentum has been recovered by the SRVs. When referring back to Fig. 5(a) of drag disabled case, it can be seen that SRVs with 4 vanes provide as much as 64.4% thrust of SRVs with 100 vanes which is considered as the maximum potential. When applying this relation to the calculation of the swirl recovery, it can be derived that 65.2% of angular momentum can be recovered by the SRVs with 100 vanes, leaving the remaining 34.8% of swirl unutilized. This results from the reason that the solidity of the SRVs is non-uniform along the radius as discussed below.

The residual swirl remains mainly within the area from 0.5R to 0.8R, where the swirl is stronger compared to the outboard region above 0.8R and the solidity is lower compared to the inboard region below 0.5R. One way to tackle this problem is to have a Y-shaped vane, of which the branches can start at the radial position of the large residual swirl area (0.5R in this case). With Y-shaped vanes, the solidity in the inboard region remains at the same level as that of the conventional vanes, while in the outboard region from, the solidity is doubled because of the introduction of the second branch. As a result, the swirl recovery potential is enhanced in this region.

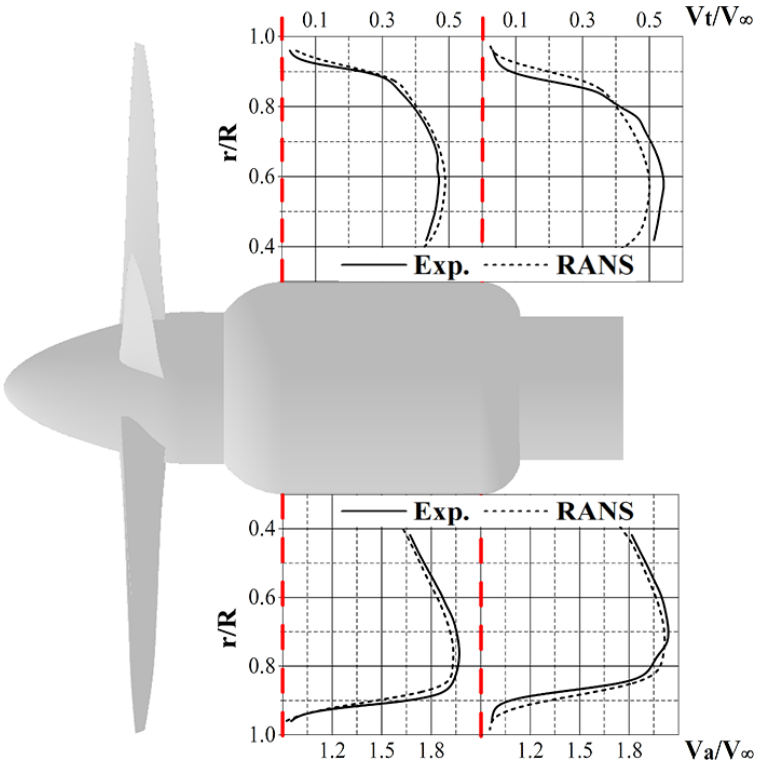

Figure 11. PIV validation of the input velocities from RANS simulation of the propeller.

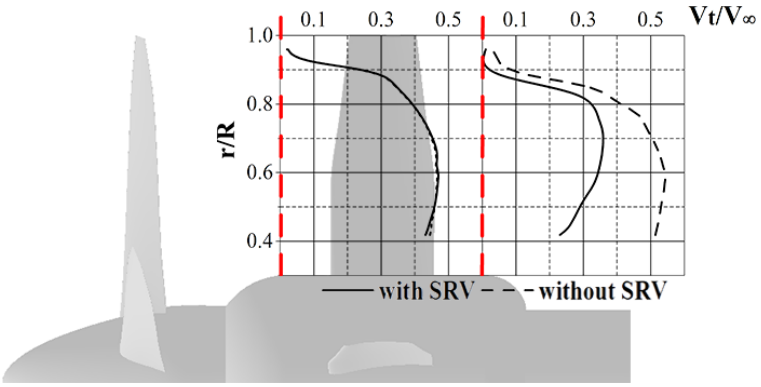

Figure 12. Quantification of swirl recovery from PIV measurements.

IV. Conclusion

A hybrid framework for SRV design was developed based on a lifting-line model. This design framework allows for a fast computation and is suitable for system level design and parameter studies, while including the detailed vane shape determination by the airfoil design procedure proposed in this paper. As a test example, a set of SRVs was designed for a six-bladed propeller and subsequently validated in a low-speed open-jet wind tunnel.

At the design point of a high propeller loading condition (J=0.6), an extra 2.6% of propeller thrust was measured from the SRVs, indicating the same amount of improvement in propeller efficiency. The thrust coefficient of the SRVs shows an approximately linear relation with the propeller advance ratio, diminishing at the cruise condition (J=1.0) to 0.8% of the propeller thrust.

The swirl recovery from the SRVs was quantified by PIV measurements, and 42% of the angular momentum in the propeller slipstream was recovered by the SRVs. The residual swirl lies mainly within the radial range of 0.5R – 0.8R where the swirl is stronger compared to the outboard region and the solidity is smaller compared to the inboard region. The swirl recovery in this region could be enhanced by applying a Y-shaped SRV design.

References

[1] International Civil Aviation Organization, *ICAO Environmental Report 2016*, < http://www.icao.int/environmental-protection/Documents/ICAO%20Environmental%20Report%202016.pdf>, 2016.

[2] Mikkelson, D. C., Mitchell, G. A., and Bober, L. J., "Summary of Recent NASA Propeller Research," *AGARD Fluid Dynamics Meeting on Aerodynamics and Acoustic of Propellers*, Toronto, Canada, 1984.

[3] Strack, W. C., Knip, G., Weisbrich, A. L., Godston, J. and Bradley, E., "Technology and Benefits of Aircraft Counter Rotation Propellers," NASA-TM-82983, 1982.

[4] Strack, W. C., Knip, G., Weisbrich, A. L., Godston, J., and Bradley, E., "Technology and Benefits of Aircraft Counter Rotation Propellers," NASA-TM-82983, 1981.

[5] Roosenboom, E. W. M., Schröder, A., Geisler, R., Pallek, D., Agocs, J., Stürmer, A., Marquez Gutierrez, C. and Neitzke, K.P., "Experimental and Numerical Investigation of a Counter Rotating Open Rotor Flow Field," *29th AIAA Applied Aerodynamics Conference*, Honolulu, HI, USA, 2011.

[6] Miller, C. J., "Euler Analysis of a Swirl Recovery Vane Design for Use with an Advanced Single-rotation Propfan," *AIAA/SAE/ASME/ASEE 24th Joint Propulsion Conference*, Boston, MA, USA, 1988.

[7] Gazzaniga, J. A., and Rose, G. E., "Wind Tunnel Performance Results of Swirl Recovery Vanes as Tested with an Advanced High Speed Propeller," *AIAA/SAE/ASME/ASEE 28th joint propulsion conference and exhibit*, Nashville TN, USA, 1992.

[8] Dittmar, J. H. and Hall, D. G., "The Effect of Swirl Recovery Vanes on the Cruise Noise of an Advanced Propeller." *13th Aeroacoustics Conference*, Tallahassee, FL, USA, 1990.

[9] Wang, Y., Li, Q., Eitelberg G., Veldhuis, L. L. M., and Kotsonis, M., "Design and Numerical Investigation of Swirl Recovery Vanes for the Fokker 29 Propeller,". *Chinese Journal of Aeronautics*, Vol.27(5),1128–1136, 2014.

[10] Stokkermans, T. C. A., van Arnhem N., Veldhuis, L. L. M., "Mitigation of Propeller Kinetic Energy Losses with Boundary Layer Ingestion and Swirl Recovery Vanes," *Royal Aeronautical Society Applied Aerodynamics conference*, Bristol, United Kingdom, 2015.

[11] Li, Q., Wang, Y., and Eitelberg, G., "An Investigation of Tip Vortices Unsteady Interaction for Fokker 29 Propeller with Swirl Recovery Vane,". *Chinese Journal of Aeronautics*, Vol.29(1), 117-128, 2016.

[12] Sinnige, T., van Kuijk, J. J. A., Lynch, K. P., Ragni, D., Eitelberg, G., and Veldhuis, L. L. M., "The Effects of Swirl Recovery Vanes on Single–Rotation Propeller Aerodynamics and Aeroacoustics," *21st AIAA/CEAS Aeroacoustics Conference*, Dallas, TX, USA, 2015.

[13] Epps B. P., "An Impulse Framework for Hydrodynamic Force Analysis: Fish Propulsion, Water Entry of Spheres, and Marine Propellers," Ph.D. Dissertation, Massachusetts Institute of Technology, Cambridge, MA, 2010.

[14] Nethrlands Aerospace Centre, "N250 propeller shoptest,".Technical report, 1989.

[15] Epps, B., Chalfant, J., Kimball, R., Techet, A., Flood, K. and Chryssostomidis, C., "OpenProp: an Open-source Parametric Design and Analysis Tool for Propellers," *Proceedings of the 2009 Grand Challenges in Modeling & Simulation Conference*, Society for Modeling & Simulation International, 2009.

[16] Drela, M., "XFOIL: An Analysis and Design System for Low Reynolds Number Airfoils," *Low Reynolds number aerodynamics*, Springer Berlin Heidelberg, 1989. 1-12.

[17] Gopalarathnam, A., Broughton, B. A., McGranahan, B. D. and Selig, M. S., "Design of Low Reynolds Number Airfoils with Trips", *Journal of aircraft*, Vol.40(4), 768-775, 2003.

[18] Lyon, C. A., Selig, M. S. and Broeren, A. P., "Boundary Layer Trips on Airfoils at Low Reynolds Numbers," *35th Aerospace Sciences Meeting & Exhibit*, Reno, NV, USA, 1997.

[19] Lignarolo, L., Ragni, D., Krishnaswami, C., Chen, Q., Ferreira, C. S., and Van Bussel, G., "Experimental Analysis of the Wake of a Horizontal-axis Wind-turbine Model", *Renewable Energy*, Vol. 70, 31-46, 2014.

[20] Howard, R. M., Miley, S. J. and Holmes, B. J., "An Investigation of the Effects of the Propeller Slipstream on a Laminar Wing Boundary Layer," (No. 850859). SAE Technical Paper, 1985.